jove

Imaging and Analysis of Neurofilament Transport in Excised Mouse Tibial Nerve

Nicholas P. Boyer[1], **Maite Azcorra**[1,2], **Peter Jung**[3,4], **Anthony Brown**[1]

[1] Department of Neuroscience, The Ohio State University [2] Present address: Interdepartmental Neuroscience Graduate Program and Department of Neurobiology, Northwestern University [3] Quantitative Biology Institute, Ohio University [4] Department of Physics and Astronomy, Ohio University

Corresponding Author

Anthony Brown
brown.2302@osu.edu

Citation

Boyer, N.P., Azcorra, M., Jung, P., Brown, A. Imaging and Analysis of Neurofilament Transport in Excised Mouse Tibial Nerve. *J. Vis. Exp.* (), e61264, doi:10.3791/61264 (2020).

Date Published

June 25, 2020

DOI

10.3791/61264

URL

jove.com/video/61264

Abstract

Neurofilament protein polymers move along axons in the slow component of axonal transport at average speeds of ~0.35-3.5 mm/day. Until recently the study of this movement in situ was only possible using radioisotopic pulse-labeling, which permits analysis of axonal transport in whole nerves with a temporal resolution of days and a spatial resolution of millimeters. To study neurofilament transport in situ with higher temporal and spatial resolution, we developed a Thy1-paGFP-NFM transgenic mouse that expresses neurofilament protein M tagged with photoactivatable GFP in neurons. Here we describe fluorescence photoactivation pulse-escape and pulse-spread methods to analyze neurofilament transport in single myelinated axons of tibial nerves from these mice ex vivo. Isolated nerve segments are maintained on the microscope stage by perfusion with oxygenated saline and imaged by spinning disk confocal fluorescence microscopy. Violet light is used to activate the fluorescence in a short axonal window. The fluorescence in the activated and flanking regions is analyzed over time, permitting the study of neurofilament transport with temporal and spatial resolution on the order of seconds and microns, respectively. Mathematical modeling can be used to extract kinetic parameters of neurofilament transport including the velocity, directional bias and pausing behavior from the resulting data. The pulse-escape and pulse-spread methods can also be adapted to visualize neurofilament transport in other nerves. With the development of additional transgenic mice, these methods could also be used to image and analyze the axonal transport of other cytoskeletal and cytosolic proteins in axons.

Introduction

The axonal transport of neurofilaments was first demonstrated in the 1970s by radioisotopic pulse-labeling[1]. This approach has yielded a wealth of information about neurofilament transport in vivo, but it has relatively low

spatial and temporal resolution, typically on the order of millimeters and days at best[2]. Moreover, radioisotopic pulse-labeling is an indirect approach that requires the injection and sacrifice of multiple animals to generate a single time course. With the discovery of fluorescent proteins and advances in fluorescence microscopy in the 1990s, it subsequently became possible to image neurofilament transport directly in cultured neurons on a time scale of seconds or minutes and with sub-micrometer spatial resolution, affording much greater insight into the mechanism of movement[3]. These studies have revealed that neurofilament polymers in axons move rapidly and intermittently in both anterograde and retrograde directions along microtubule tracks, propelled by microtubule motor proteins. However, neurofilaments are diffraction-limited structures just 10 nm in diameter that are typically spaced apart from their neighbors by only tens of nanometers; therefore, the polymers can only be tracked in cultured neurons that contain sparsely distributed neurofilaments so that the moving polymers can be resolved from their neighbors[4]. Thus, it is not presently possible to track single neurofilaments in axons that contain abundant neurofilament polymers, such as myelinated axons.

To analyze the axonal transport of neurofilaments in neurofilament-rich axons using fluorescence microscopy, we use a fluorescence photoactivation pulse-escape method that we developed to study the long-term pausing behavior of neurofilaments in cultured nerve cells[4,5]. Neurofilaments tagged with a photoactivatable fluorescent neurofilament fusion protein are activated in a short segment of axon, and then the rate of departure of those filaments from the activated region is quantified by measuring the fluorescence decay over time. The advantage of this approach is that it is a population-level analysis of neurofilament transport that can be applied on a time-scale of minutes or hours without the need to track the movement of individual neurofilament polymers. For example, we have used this method to analyze the kinetics of neurofilament transport in myelinating cultures where the axons contain abundant neurofilaments, and it is not possible to resolve individual neurofilament polymers[6].

Recently, we described the development of a hThy1-paGFP-NFM transgenic mouse that expresses low levels of a paGFP-tagged neurofilament protein M (paGFP-NFM) in neurons under the control of the human neuron-specific Thy1 promoter[7]. This mouse permits the analysis of neurofilament transport in situ using fluorescence microscopy. In this article, we describe the experimental approaches for analyzing neurofilament transport in myelinated axons of tibial nerves from these mice using two approaches. The first of these approaches is the pulse-escape method described above. This method can generate information about the pausing behavior of the neurofilaments, but is blind to the direction which the filaments depart the activated region, and therefore does not permit measurement of the net directionality and transport velocity[8]. The second of these approaches is a new pulse-spread method in which we analyze not just the loss of fluorescence from the activated region, but also the transient increase in fluorescence in two flanking windows through which the fluorescent filaments move as they depart the activated region in both anterograde and retrograde directions. In both approaches, parameters of neurofilament transport such as the average velocity, net directionality and pausing behavior can be obtained by using mathematical modeling of the changes in fluorescence in the measurement windows. **Figure 2** illustrates these two approaches.

This protocol demonstrates the dissection and preparation of the nerve, activation and imaging of paGFP fluorescence, and quantification of neurofilament transport from the acquired

images using the FIJI distribution package of ImageJ[9]. We use the tibial nerve because it is long (several cm) and does not branch; however, in principle any nerve expressing paGFP-NFM is appropriate for use with this technique if it can be dissected and de-sheathed without damaging the axons.

Protocol

All methods described here have been approved by the Institutional Animal Care and Use Committee (IACUC) of The Ohio State University.

1. Preparation of nerve saline solution

1. Make 100 mL of Breuer's saline[10]: 98 mM NaCl, 1 mM KCl, 2 mM KH_2PO_4, 1 mM $MgSO_4$, 1.5 mM $CaCl_2$, 5.6% D-glucose, 23.8 mM $NaHCO_3$ in double-distilled water.
2. Bubble 95% oxygen/5% carbon dioxide (carbogen) through the saline solution for at least 30 minutes prior to use. Leftover saline can be reused within one week; however, it must be reoxygenated before each use.
3. Pour oxygenated saline into a 60 mL syringe and ensure that there is minimal air remaining in the syringe.

2. Initial assembly of nerve perfusion chamber

1. Connect the syringe and the tubing as shown in **Figure 1A**, placing the outflow tube into a waste flask.
2. Place the outer gasket into the perfusion chamber housing, ensuring that the flow inlet and outlet posts are aligned with the holes in the gasket.
3. Lay the inner gasket (silicone, 100 µm thick) on a #1.5 circular coverslip (40 mm diameter), carefully smoothing out any wrinkles in the gasket to ensure a tight seal. To facilitate later assembly, place the coverslip and gasket on a paper towel or task wipe with the gasket facing up.

3. Dissection and preparation of mouse tibial nerve

1. Sacrifice the animal by carbon dioxide inhalation or another institutionally approved method. Start a timer when the animal ceases movement/breathing, as experiments must only be conducted within 3 hours of sacrifice[7].
2. Spray the fur with 70% ethanol and remove as much as possible from the animal's legs and back using an electric razor.
3. Using a pair of large dissection scissors, make a dorsal incision in the skin near the middle of the spine and continue the cut around the ventral aspect of the animal. Starting from this cut, slowly reflect the skin from the legs by gently pulling it away from the muscle and cutting the fascia.
4. Place the animal in a supine position on a dissection tray and pin all four paws. Optionally pin the tail to reduce movement further.
5. Using microdissection scissors, make an incision in the thigh muscles midway between the tail and knee to expose the sciatic nerve. Ensure that the nerve, which is visible through the muscle, is not cut.
6. Extend the incision dorsally and ventrally to remove the muscle. Similarly, remove the muscles of the calf, keeping cuts shallow and short to avoid damaging nerves.
7. Remove muscles until the tibial nerve is fully exposed from the point where it branches from the sciatic nerve (at the knee) to the heel (**Figure 1B**).

NOTE: In all steps including and following dissection of the tibial nerve, avoid unnecessary exposure to ambient light to minimize possible incidental activation of paGFP in the nerve.

8. Grasp the tibial nerve at the spine-proximal end with a pair of forceps and cut the nerve using a pair of microdissection scissors. Taking care not to put tension on the nerve, lift it away from the muscle, cutting any attachments.

9. Cut the spine-distal end of the tibial nerve and transfer to a small Petri dish of room temperature oxygenated saline. From this point on in the procedure, always be certain to keep track of the proximal and distal ends of the nerve.
NOTE: One way to do this is to mark the distal end of the nerve with an angled cut such that the taper is visible.

10. Starting from the proximal end of the nerve, gently grasp the exposed axon ends with a pair of very fine-tipped forceps.

11. With a second pair of forceps, grasp the nerve sheath proximally, and slowly pull towards the distal end of the nerve. The nerve sheath will slide along the axons with minimal resistance. Ensure that no undue tension is applied to the nerve during this process.

4. Final nerve perfusion chamber assembly

1. Remove the nerve from the saline and quickly lay it on the circular coverslip of the perfusion chamber within the rectangular opening of the inner gasket. Grasping the proximal end of the nerve, slowly lay it down onto the coverslip under gentle tension to straighten the nerve.

2. Place the microaqueduct slide over the nerve with the grooved side facing the nerve, and the direction of flow parallel to the nerve so that the nerve and surrounding inner gasket are now sandwiched between the coverslip and the microaqueduct slide. Flip the coverslip and microaqueduct assembly over, and place it within the perfusion chamber housing with the microaqueduct slide apposed to the outer gasket. The nerve will now be sandwiched between the coverslip and the microaqueduct slide, which are separated by the silicone gasket, with the coverslip facing up (**Figure 1B**).

3. Secure the perfusion chamber by placing it in the metal housing and rotating the locking ring. Ensure that the plastic housing is fully under all metal clips and tighten well to prevent saline leakage. Overtightening may crack the microaqueduct slide or coverslip. Flip the chamber over so that the coverslip is facing down.

4. Slowly depress the saline syringe plunger to fill the perfusion chamber. Keep the inlet and outlet tubing, outlet flask and syringe elevated above the chamber itself at all times during setup and imaging. This avoids siphoning, which can cause introduce bubbles or cause focus instability due to negative pressure in the chamber.

5. Transfer the perfusion assembly to an inverted microscope stage and mount the saline syringe into the syringe pump. Start the motor at an appropriate speed for a flow rate of 0.25 mL/min. Then connect and turn on the in-line solution heater set to 37 °C.

6. Connect the objective heater and set to 37 °C, apply oil to the objective, and insert the perfusion chamber into the stage mount.

7. Apply oil to the chamber heater pad and attach to the perfusion chamber. Connect and turn on the chamber heater; set to 37 °C.
NOTE: Changes in temperature may cause bubbles to form in the perfusion chamber due to outgassing of the

solution. If bubbles form, briefly increase the solution flow rate by 5-10x until bubbles clear the chamber.

8. Lock the perfusion chamber into the stage adapter and bring the objective oil into contact with the coverslip on the underside of the chamber.

   NOTE: The Bioptechs chamber with ASI stage adapter used here are designed for an inverted microscope configuration.

5. Fluorescence activation and image acquisition

1. Using brightfield illumination, focus on the layer of axons on the bottom surface of the nerve closest to the coverslip surface (**Figure 1C**). Myelinated axons (typically 1 - 6 µm in diameter in adult mice) can be identified by the presence of a myelin sheath, which is visible under brightfield transmitted light illumination without contrast enhancement. Schmidt-Lanterman clefts and nodes of Ranvier are also readily apparent. Unmyelinated axons are more slender (typically <1 µm diameter) and are generally present in bundles (Remak bundles), where they are generally too closely apposed to be resolved from each other.

2. If available on the microscope, activate the auto-focus system to maintain focus over the course of timelapse imaging.

3. Acquire a brightfield reference image. Record the directionality of the nerve (spine-proximal and distal ends) with respect to images.

4. Acquire a confocal image using a 488 nm laser and an emission filter appropriate for paGFP (e.g., 525/50 nm). Keep the laser power low to minimize photobleaching, with exposure time adjusted accordingly to detect the faint signal. As an example, representative data were acquired at 5% laser power and 4 s exposures. Record the acquisition settings for use in all future experiments.

   NOTE: After photoactivation, the ideal imaging settings will produce a signal-to-noise ratio > 8 and photobleaching of less than 25% of the original signal over the course of 20 images. The axons can also be imaged by widefield epifluorescence microscopy as we did originally[7], but the image quality will be inferior due to lack of confocality.

5. Set the laser power to approximately 5x normal imaging power and acquire an image with an exposure time of 3-4 minutes. Though not essential, this step is recommended to bleach autofluorescence and other sources of unwanted fluorescence in order to reduce background signal and thus maximize the signal-to-noise of the photoactivated fluorescence.

6. Acquire an image with the settings used in step 5.4 to record the pre-activation autofluorescence after this bleaching step.

7. On the brightfield image, draw a line parallel to the axons with a length equal to desired activation window size. The size of this window will vary depending on the experimental goal and parameters, but typical sizes are 5 µm for the pulse-escape paradigm and 40 µm for the pulse-spread paradigm.

8. Using this line as a guide, draw a rectangular region of interest (ROI) across the field of view perpendicular to the axons. The region must encompass all the axons to be photoactivated.

9. Determine optimal settings for photoactivation with 405 nm illumination.

   NOTE: Only perform this step and sub-steps prior to first experimental activation. Over the course of an

experiment, the same photoactivation settings must be used.

1. Activate a region of interest repeatedly using the 405 nm laser line, low laser power (e.g., 5%), pixel dwell time (e.g., 40 µs), and one pulse, acquiring an image of the activated GFP fluorescence after each activation. Repeat until the fluorescence no longer increases, and then quantify the fluorescence in a region of interest for each image.
2. Plot the average fluorescence intensities versus pulse number. Select the number of pulses after which fluorescence no longer increases as the optimal setting for activation.

10. Activate the paGFP fluorescence in this region by patterned excitation with 405 nm light. Ensure that an image is acquired just prior to and just following activation.
    NOTE: The ideal paGFP activation will produce a clearly defined region of fluorescence with sharp boundaries contained within the ROI.
11. Start a 1 minute timer as the activation finishes. At the end of 1 minute, start acquisition of a timelapse series.
    NOTE: The 1 minute delay is necessary to allow for the increase in fluorescence that is observed following photoactivation of paGFP[11]. For the pulse-spread method, a 5 minute acquisition period with 30 second timelapse intervals is sufficient for measurement of the initial slopes in the central and flanking windows to measure velocity and directionality. For the pulse-escape method, an acquisition period of 30-150 minutes with 5 or 10 minute timelapse intervals permits analysis of the long-term pausing behavior of the filaments
12. Save all images acquired, as well as the ROI used for fluorescence activation.
13. Move to a new region of the nerve and repeat steps 5.1-5.11. If the new region is along the same axon, it must be at least 500 µm from the previously activated region to avoid detection of fluorescent neurofilaments that moved out of the other activated region. The acquisition of the final timelapse must finish before the end of the 3 hour window.
    NOTE: It is possible that the preparation may be viable for longer than 3 hours, but we have not confirmed that. With proficient dissection and preparation, between five and eight 10-minute timelapse image sets may be acquired within this 3 hour window.
14. After the final timelapse image series is acquired, stop the flow of saline, disconnect the solution and chamber heaters, and remove the perfusion apparatus from the microscope stage.

6. Flatfield and darkfield image acquisition

1. Make a solution of fluorescein by adding 250 mg of fluorescein powder to 0.5 mL of double distilled water. Mix until there are no visible particles and spin the solution for 30 seconds in a tabletop centrifuge to sediment any undissolved material. This solution can be stored for several months at 4 °C if protected from light exposure.
2. Add 8 µL of fluorescein solution to a slide and apply a #1.5 coverslip. Blot excess liquid, seal with nail polish, and allow to dry.
   NOTE: At this high concentration, the strong absorption of the fluorescein dye extinguishes the illuminating beam within the solution, producing a thin plane of fluorescence at the surface of the coverslip that is both uniform and resistant to photobleaching due to rapid diffusive exchange[12].

3. Place the fluorescein slide coverslip-side down on the inverted microscope stage and adjust the focus on the thin plane of fluorescence at the surface of the coverslip. Move around the slide to find a field of view that does not contain air bubbles (dark spots) or large fluorescein particles (bright spots).

4. Acquire a z-stack spanning 6 µm at 0.2 µm intervals such that the middle image is the original focus plane. Use a short exposure time (e.g., 40 ms) because the fluorescence will be very bright. This z-stack acquisition is necessary to capture the maximal fluorescence across the field of view as the coverslip is rarely perfectly horizontal and the plane of fluorescein fluorescence is very narrow. Repeat this for a total of 25 fields of view, moving the stage by at least 20 µm in any direction between images.

5. Close all light path shutters, including the camera shutter, and set the laser power and the exposure time to 0 s. Acquire a stack of 100 images with these settings. These images will be averaged to generate the darkfield image, which will be used to correct for dark current and the bias offset on the camera chip.

   NOTE: Streaming acquisition is an ideal way to capture these images.

7. Imaging glycolytically inhibited nerves for bleach correction

1. Make and oxygenate a saline solution as in step 1; however substitute 2-deoxy-D-glucose for D-glucose and add 0.5 mM sodium iodoacetate to inhibit glycolysis[13]. We refer to this as “inhibitory saline”.

2. Repeat steps 2-5 using the inhibitory saline, with a 10-30 minute timelapse image set in step 5.11. Allow 40-50 minutes after application of inhibitory saline before imaging to ensure complete inhibition of neurofilament transport.

   NOTE: Glycolytic inhibition will eventually kill the axons so there is a narrow window of time after inhibition in which to acquire data, typically about 30 minutes. An indicator of the level of metabolic inhibition is the flavin autofluorescence of the axonal mitochondria, which can be detected in the timelapse series due to the long exposures that we use to image the paGFP fluorescence[14]. Typically, mitochondrial autofluorescence will become readily apparent by 70-80 minutes after applying inhibitory saline and increases over time. If the mitochondria begin to round up or fragment, and then cease imaging.

8. Image processing and analysis using ImageJ

1. Flatfield and darkfield correction

   1. Open the darkfield image stack and average the images by clicking **Image | Stacks | Z Project** and selecting **Average Intensity** in the drop-down menu to generate the **darkfield** image.

   2. Open the fluorescein flatfield image stacks and create a maximum intensity projection of each (25 in total) by clicking **Image | Stacks | Z Project** and selecting **Max Intensity** in the drop-down menu.

   3. Combine the resultant 25 maximum projection images into one stack by clicking **Image | Stacks | Images to Stack**. Create an average intensity projection of this stack by clicking **Image | Stacks | Z Project** and selecting **Average Intensity** from the dropdown menu to generate the **flatfield image**.

4. Subtract the darkfield image from the flatfield image by clicking **Process | Image Calculator**, selecting **Subtract** as the operation. Ensure that the **32-bit (float) result** option is checked. The result is the **corrected flatfield image**.

5. Measure the average pixel intensity of the corrected flatfield image by first clicking **Analyze | Set Measurements** and checking the **Mean gray value** box, and then pressing the 'm' key.

6. Divide the corrected flatfield image by its average intensity by clicking **Process | Math | Divide** and entering the average gray value obtained in step 7.1.5. This will produce the **inverse gain** image.

7. Open the pre-activation and post-activation images along with the timelapse image stack. Combine the images into a single stack by clicking **Image | Stacks | Tools | Concatenate**, and select the images in chronological order from the dropdown menus. Make sure that the **Open as 4D image** option is not selected. The resulting stack is the **full image set**.

8. Repeat step 8.1.4 on the **full image set**, and then divide the result by the **inverse gain** image by clicking **Process | Image Calculator** and selecting **Divide** as the operation. This will produce the **corrected full image set**, in which each image has been corrected for the non-uniformity in the field of illumination and on the detector.

2. Image stack alignment

1. To correct for misalignment of the image planes in the timelapse series due to stage or sample drift, install the **Alignment by fixed region** plugin (**Supplemental File 1**) by clicking **Plugins | Install PlugIn**, navigating to the folder containing the plugin file, and selecting the plugin. Restart ImageJ after installing the plugin.

   NOTE: This plugin aligns images based on the "least squares congealing" principle[15] .

2. Draw an ROI on the **corrected full image set** which spans several axons and does not extend beyond the proximal and distal boundaries of the activated fluorescence within each of the axons. The geometry of the region is unimportant, however excluding areas in which structures change shape or size will improve alignment.

3. Run the alignment plugin by clicking **Plugins | Alignment by fix region**. The plugin places a default 2-pixel maximum on displacement between frames, however this may be adjusted in the initial popup window if there is significant drift of the sample. The alignment may take several minutes, depending on the size of the image stack.

4. Visually inspect the aligned stack to assess the quality of the alignment. Some frames may then need to be aligned manually, as the automated alignment may not function well for large fluctuations in fluorescence between frames. This may be accomplished while viewing a frame which must be shifted by clicking **Image | Transform | Translate**. Click **No** on the following popup asking whether the entire stack should be translated.

5. Save this as the **aligned full image set**. Use only integer pixel values in translation and ensure that the dropdown interpolation menu is set to **None**, as fractional pixel shifts or interpolation will alter the data due to resampling of the pixel intensities.

3. Measurement of fluorescence intensities

1. Draw an ROI using the Angle tool on the first frame of the **aligned full image set** with the first arm along one edge of the activated region, perpendicular to the axons, and the second arm vertical. Press the 'm' key to measure the angle, which describes the orientation of the axons in the field of view.
2. Set the scale of the images so that dimensions are measured in microns by clicking **Analyze | Set** Scale and entering the appropriate values.
3. Open the ROI manager by clicking **Analyze | Tools | ROI Manager**. For pulse-escape paradigm, skip to step 8.3.7. For pulse-spread, continue to step 8.3.4.
4. Draw a square ROI of any dimensions, and then click **Edit | Selection | Specify**. Ensure that the **Scaled** units option is checked, and then set the ROI to a width of 15µm and a height equal to or greater than the height of the image.
5. Rotate the ROI by the angle measured in step 8.3.1 by clicking **Edit | Selection | Rotate** to make it perpendicular to the axons, and place the ROI with one side along the proximal edge of the activated region. Add this ROI, which we will refer to as the proximal guide ROI, to the manager by pressing the 't' key.
6. Drag the ROI to align with the distal edge of the activated region and add to the ROI manager again by pressing the 't' key. We will refer to this as the distal guide ROI. The proximal and distal guide ROIs will be used later to draw the flanking measurement ROIs.
7. Select axons for quantification, using the timelapse image, acquired in step 5.10 above. This image is helpful for this purpose because it captures the weak autofluorescence of the axons, revealing their morphology outside of the activated region.

   NOTE: Axons that do not meet the following criteria are excluded from the analysis:

   - Axons must be in focus along the entire length of all measurement windows.
   - Axons must be within 5° of perpendicular to the edges of the activation region.
   - Axons must have no invaginations within 5µm of the edges of the activation region.
   - Exclude axons which change shape visibly during the course of imaging.
   - Exclude axons that appear unhealthy as evidenced by the absence of a discrete activated region in the post-activation image (**Figure 1D**, top), as this is indicative of diffusive dispersion of the activated fluorescence, which happens when the axon dies.
8. Observe long-exposure bleaching image for autofluorescent structures within axons. This fluorescence is due to flavins within mitochondria[16]. Exclude axons from analysis if these mitochondria appear rounded or fragmented (**Figure 1E**, top), as opposed to extended, linear structures (**Figure 1E**, bottom), as this is an indication of metabolic decline.
9. Using the proximal and distal guide ROIs created above, draw three measurement ROIs per axon being analyzed: a central window encompassing the axon within the 40 µm activated region, and two flanking windows with width constrained by flanking window 15 µm ROIs and height constrained by the diameter of the axon at the border of the activation region. Add all three regions to the ROI manager. For the

pulse-escape paradigm, only the 5 µm central region is needed. For glycolytically inhibited axons, draw a single region no more than 5 µm wide in the middle of the activated region that does not extend outside the axon.

10. Repeat step 8.3.9 for all axons which meet criteria of steps 8.3.7 and 8.3.8.

11. Set active measurements to average pixel intensity by clicking **Analyze | Set Measurements** and selecting the **Mean gray value** option. Ensure that no other measurement options are checked.

12. Select all ROIs in the ROI Manager window by selecting the window and pressing 'Ctrl' + 'a'. In the ROI Manager window, click **More | Multi Measure** to measure the fluorescence intensities. Copy the data from the results window to a spreadsheet for further analysis.

13. Set active measurements to region area by clicking **Analyze | Set Measurements** and selecting the **Area** option. Ensure that no other measurement options are checked.

14. Repeat step 8.3.12. It is only necessary to copy one row of the results for the area, as the area does not vary with time.

9. Photobleach correction

1. In the data spreadsheet for glycolytically inhibited axons, subtract the mean fluorescence of frame 1 (the pre-activation frame) from the mean fluorescence of each frame starting at frame 3 (the first timelapse frame) for a given ROI. The results are the **background-subtracted means**.

2. Plot the data as a scatterplot with the frame numbers as the abscissa. Fit an exponential trendline to the data from each ROI (most spreadsheet programs have this function) with an equation in the form of $\mathbf{Ae^{-bx}}$. This equation is equivalent to the photobleaching function $F_t = F_0 * e^{-\gamma t}$ where F_0 is the fluorescence at the first frame of the timelapse, γ is the exponential bleaching rate, t is the time, and e is the natural logarithm base.

3. Repeat steps 9.1.1-9.1.2 for all ROIs of all axons from the glycolytically inhibited nerves. For the most accurate estimate of the photobleaching rate, use at least 15 axons in total from at least 5 separate nerves. Use the average of the exponential bleaching rates (γ) from all inhibited axons to correct the experimental data for photobleaching. A new bleaching calibration must be performed for each experiment or study, because photobleaching is dependent on the image acquisition settings and the laser power, which can change over time.

4. Repeat step 9.1.1 for all regions of axons imaged with normal saline (i.e. not glycolytically inhibited).

5. Divide each data point by $e^{-t\gamma}$, using time for t and the average γ found in step 9.1.3. These are the **photobleach-corrected means**.

6. Multiply each data point by the area for that region of interest to find the **total fluorescence** in that region at each time.

Representative Results

Figure 3 shows representative images from pulse-escape and pulse-spread experiments. We have published several studies that describe data obtained using the pulse-escape method and our methods for the analysis of those

data[5,6,7,8,17]. Below, we show how the pulse-spread data can yield information on the directionality and velocity of neurofilament transport, which we have not reported previously.

Neurofilament transport in the axon is intermittent and bidirectional. This transport can be described by the fraction of filaments moving at any given time in the anterograde and retrograde directions, P_a and P_r respectively, and their velocities in the anterograde and retrograde directions, denoted by v_a and v_r. If we take the total quantity of neurofilament polymer per unit length of axon to be n, and then the fluxes in the anterograde and retrograde directions through a given region are given by

$$j_a = np_a v_a$$

and

$$j_r = -np_r v_r ,$$

respectively, and the total flux j is given by

$$j = j_a + j_r = n(p_a v_a - p_r v_r) ,$$

where n has units μm^{-1}, v has units $\mu m \cdot s^{-1}$ and j has units s^{-1}. Since the flux at a given location along the axon is the quantity of neurofilament polymer that moves past that location in a unit of time, it is related to the average velocity $\bar{v}$ through $j = n\bar{v}$. Thus, we can write

$$\bar{v} = p_a v_a - p_r v_r .$$

In a pulse-spread experiment the flux can be determined from the rate of departure of the fluorescent neurofilaments from the activated region, which we refer to as the central window. The total loss of fluorescent neurofilament polymer from this central window per second $(\frac{dQ_c}{dt})$ is the sum of the losses due to fluorescent neurofilament polymers leaving in anterograde and retrograde directions, i.e.

$$\frac{dQ_c}{dt} = -(v_a p_a + v_r p_r)n.$$

Normalized to the initial content of fluorescent neurofilament polymer in the central window, i.e. $Q_c(0) = na$, where a is the length of the central window, this rate of loss then becomes

$$\frac{d\bar{Q}_c}{dt} = \frac{-v_a p_a + v_r p_r}{a} \equiv -S_c$$

where $-S_c$ is the slope of the decrease in fluorescence in the central window, which is initially linear for a time period given by a/v[8]. For a 40 μm central window, this equates to just tens of seconds. However, for windows this large, the transition to the exponential decay phase is gradual and the slope is effectively linear for several minutes or more[8].

At early times, the flanking windows capture all the neurofilaments that exit the central window because these filaments do not have sufficient time to pass through the flanking windows and exit them on the other side. In this case, the quantities of fluorescent neurofilament polymer that leave the central window anterogradely and retrogradely per second, i.e. the fluxes j_a and j_r, are given by the increase in the neurofilament content Q_p and Q_d in the flanking windows. Normalized to the initial content of fluorescent neurofilament polymer in the central window, the rates of increase in the flanking windows become

$$\frac{d\bar{Q}_p}{dt} = -j_r/na = \frac{p_r v_r}{a} \equiv S_p$$

$$\frac{d\bar{Q}_d}{dt} = j_a/na = \frac{p_a v_a}{a} \equiv S_d$$

where S_p and S_d are the slopes of the increase in fluorescence in the proximal and distal flanking windows, respectively.

Thus, we can express the average velocity in terms of the slopes in the flanking windows, i.e.

$$\bar{v} = a(S_d - S_p), \qquad \text{(Eq. 1)}$$

and the ratio of the number of anterograde and retrograde moving neurofilaments in terms of the ratio of these slopes, i.e.

$$\frac{p_a}{p_r} = \frac{S_d}{S_p}\frac{v_r}{v_a} = \frac{\gamma_{ra}}{\gamma_{ar}}, \qquad \text{(Eq. 2)}$$

where γ_{ar} and γ_{ra} denote the rates at which neurofilaments reverse from anterogradely to retrogradely moving and vice versa[8]. The values of v_a and v_r can be determined by measuring the movement of individual neurofilaments in cultured neurons, as reported previously[17]. Importantly, the expression for the velocity in Eq. 1 only applies at short times after activation during which fluorescent neurofilaments enter the flanking window but do not leave. The duration of this short time window will depend on the length of the flanking windows and the kinetics of the neurofilament movement. The longer the flanking windows, in principle, the longer the time window. Theoretically, one can test that this criterion is met by confirming that

$$-S_c = S_p + S_d. \qquad \text{(Eq. 3)}$$

In contrast to the expression for the velocity, which is given by the difference between the slopes in the flanking windows, the expression for the directionality in Eq. 2 is robust to flanking window size because it is given by the ratio of the slopes in the flanking windows.

Figure 3 shows representative results from pulse-escape and pulse-spread experiments on myelinated axons in the tibial nerve of an 8-week old male mouse from our Thy1 paGFP-NFM line on a C57Bl/6J background, using window sizes of 5 and 40 µm, respectively. Mice of at least 2 weeks of age, both male and female, have been used for these experimental paradigms, and the appropriate age and sex of mice should be determined by the researcher depending on what is being tested in the study. Over time, it can be seen that the edges of the activated regions blur due to the departure of neurofilaments in both anterograde and retrograde directions, resulting in loss of fluorescence from the central window.

For the pulse-escape method (**Figure 3A, C, E**), the fluorescence decay kinetics in the activated region can yield information on the long-term and short-term pausing behavior[8, 18]. For these experiments, the activated region can be short (we typically use 5 µm; see yellow box in **Figure 3A**). For the pulse-spread method (**Figure 3B, D, F**), we use a longer activated region (40 µm here; see yellow box in **Figure 3B**) in order to provide a larger pool of fluorescent neurofilaments. This lengthens the time over which the fluorescence increase in the flanking regions remains linear (see above). The linear domain of this fluorescence increase in the flanking windows can also be increased by increasing the length of these windows, however this is limited by the size of the field of view. We used 15 µm flanking windows, shown in red and green, for the data shown in **Figure 3D**.

Figure 3E,3F shows the quantification of the total fluorescence intensities (i.e., the sum of the pixel intensities) for the measurement windows shown in **Figure 3C,3D** respectively. For the pulse-escape method the decay is

biphasic, with an initial exponential decay which represents the departure of on-track neurofilaments. This transitions at around 10-20 minutes to a second slower exponential decay that represents the mobilization and departure of off-track filaments[8]. For comparison with the pulse-spread method, we show only a 12 minute time course in **Figure 3E**, but usually the time course of the analysis needs to be longer (typically 30-120 minutes) to capture the long-term pausing kinetics[5,6,18]. For the pulse-spread strategy, the calculations of the velocity and directionality of the movement are dependent only on the slopes in the flanking windows. For the window lengths used here, the linear phase extends for about 5 minutes. The duration of this time window of linearity should be assessed by incrementally shortening the time used to measure the slope, and determining the point at which the slope no longer increases. This duration can be increased by increasing the window lengths if the camera field of view permits, though the window lengths should be held constant for all axons in a given experiment. As an example, we have used the first 5 minutes of data to measure the slopes for the pulse-spread data in **Figure 3F**, along with 11 other axons in the same nerve for a total of 14 axons. This results in slopes of 72 A.U./min, 594 A.U./min, and 111 A.U./min for the proximal, central and distal windows, respectively (A.U. = arbitrary units). In order to normalize these values, they are divided by the initial fluorescence of the central window, resulting in rates of 0.108 $\%F_0$/min, -0.962 $\%F_0$/min and 0.173 $\%F_0$/min. Applying Eq. 3 we find that the conservation criterion is not met, indicating that we are not capturing all of the fluorescence in the flanking windows. This is a technical limitation due to the field of view of our EMCCD camera (82 µm x 82 µm). Cameras with sCMOS chips, which can have much larger fields of view, could permit the use of larger flanking window sizes. However, we cannot exclude the possibility that this discrepancy between the central and flanking slopes could also be due, at least in part, to underestimation of the extent of photobleaching (see Discussion), which would have the effect of underestimating the positive slopes in the flanking windows and overestimating the negative slope in the central window.

From the rates in the flanking windows ($\%F_0$/min) and Eq. 2 above, and using values of v_a = 0.9 µm/s and v_r = 1.2 µm/s[17], we calculate the ratio p_a/p_r = 2.12. This indicates that 68% of the filaments were moving anterograde and 32% retrograde. Using the same rates and Eq. 1 above, we calculate the average net population velocity v = 40*(0.00173-0.00108) = 0.026 µm/min, or 0.037 mm/day. Radioisotopic pulse-labeling studies in mice of similar age have reported a neurofilament population velocity of approximately 0.6 mm/day in the most proximal portions of the sciatic nerve, slowing to 0.12 mm/day over a distance of two centimeters[19,20]. The data was gathered in the tibial nerve, roughly another 2-3 centimeters distal to these measures. For the reasons mentioned above, we believe that the estimate of 0.037 mm/day is an underestimate of the true velocity. However, extrapolating the spatial slowing observed by radioisotopic pulse-labeling into the tibial nerve this estimate is remarkably close given that it was determined using a very different methodology on a very different spatial and temporal scale.

To demonstrate the capability of detecting significant differences between populations using the pulse-spread method, we compared the proximal and distal flanking window slopes measured from nerves perfused with both normal and inhibitor salines. Inhibition of glycolysis blocks movement of neurofilaments, as we have reported previously[5,6,7]. We will discuss later the selection of sample sizes for experiments, however here we used one

nerve in normal saline and two in inhibitor saline, due to the limitation of one acquisition field per nerve during inhibition. **Figure 4A** shows an example timelapse from a glycolytically inhibited nerve, demonstrating an apparent reduction in transport out of the activated region. Indeed, we find significantly lower distal and proximal slopes (**Figure 4B**, p = 0.61264160 and 0.00607, respectively, Tukey's pairwise comparison following ANOVA) in nerves treated with inhibitor versus those perfused with normal saline. We also find a significant decrease in the population velocity between these two conditions (**Figure 4C**, p = 0.0232, t-test with unequal variances, following F test for equal variance with p = 0.0190).

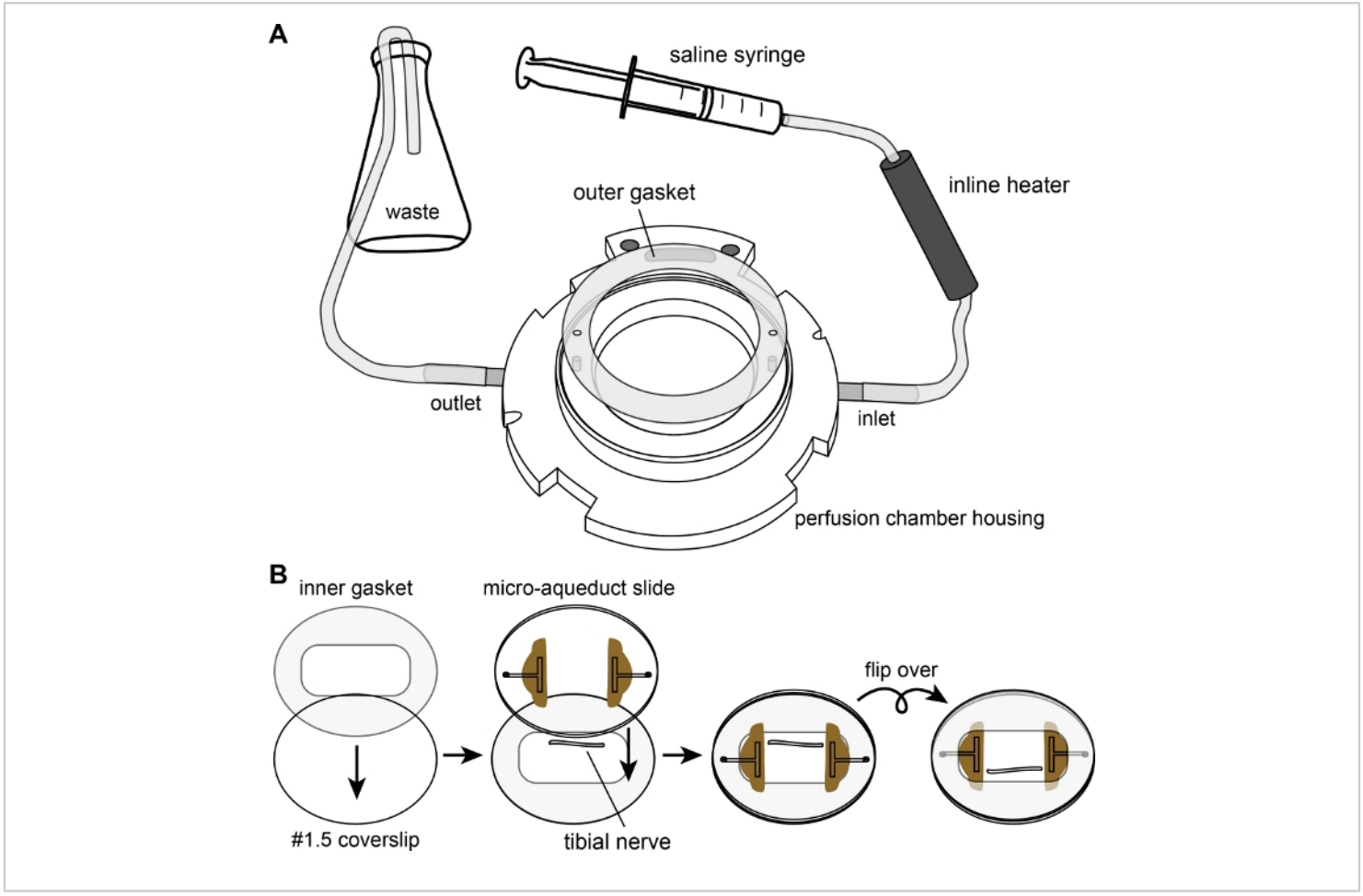

Figure 1: The perfusion chamber. (**A**) Diagram showing the assembly of the perfusion chamber housing and the outer gasket, with tubing connected to the saline syringe and waste flask. (**B**) Diagram showing the assembly of the chamber itself. The inner gasket is laid flat on top of the #1.5 coverslip. The nerve is placed on the coverslip in the well created by the rectangular opening of the inner gasket. The microaqueduct slide is placed over the nerve to sandwich the nerve between the #1.5 coverslip and the microaqueduct slide. Finally, the sandwich is flipped before mounting on top of the outer gasket of the assembly shown in (**A**) and secured with a locking ring (not shown). Please click here to view a larger version of this figure.

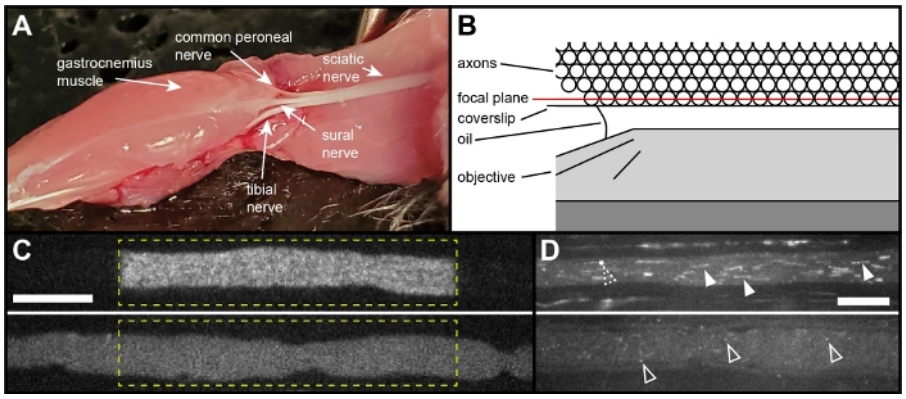

Figure 2: The tibial nerve preparation. (**A**) Image showing the location of the tibial nerve within the leg of a mouse, in which the gluteus superficialis, biceps femoris, semitendinosus, popliteus, tibialis caudalis and flexor digitorum longus muscles have been removed. The tibial nerve can be seen as one of three major branches of the sciatic nerve arising at the knee. (**B**) Schematic of the nerve in cross-section in the assembled chamber, showing the oil-immersion objective beneath the coverslip. The best optical quality is obtained by activating and imaging the layer of axons apposed to the surface of the coverslip; image quality declines deeper into the nerve due to light scattering. (**C**) Examples of a healthy axon (top), and of an unhealthy axon (bottom) immediately after activation. The dashed yellow line marks the activated region. The activated fluorescence has sharp boundaries in the healthy axon whereas in the unhealthy axon the activated fluorescence diffuses rapidly out of the activated region, filling the axon within seconds. Scale bar = 10 µm. (**D**) Examples of the mitochondrial appearance in a healthy axon (top) and an unhealthy axon (bottom). The mitochondria are visible due to flavin autofluorescence[16] . They appear linear (solid arrowheads) in healthy axons. In unhealthy axons, the mitochondria first become punctate (open arrowheads) and then subsequently fainter over time, providing an indicator of axon health. The dashed open arrowhead in the healthy axon points to a mitochondrion transitioning from linear to punctate. Scale bar = 10 µm. Please click here to view a larger version of this figure.

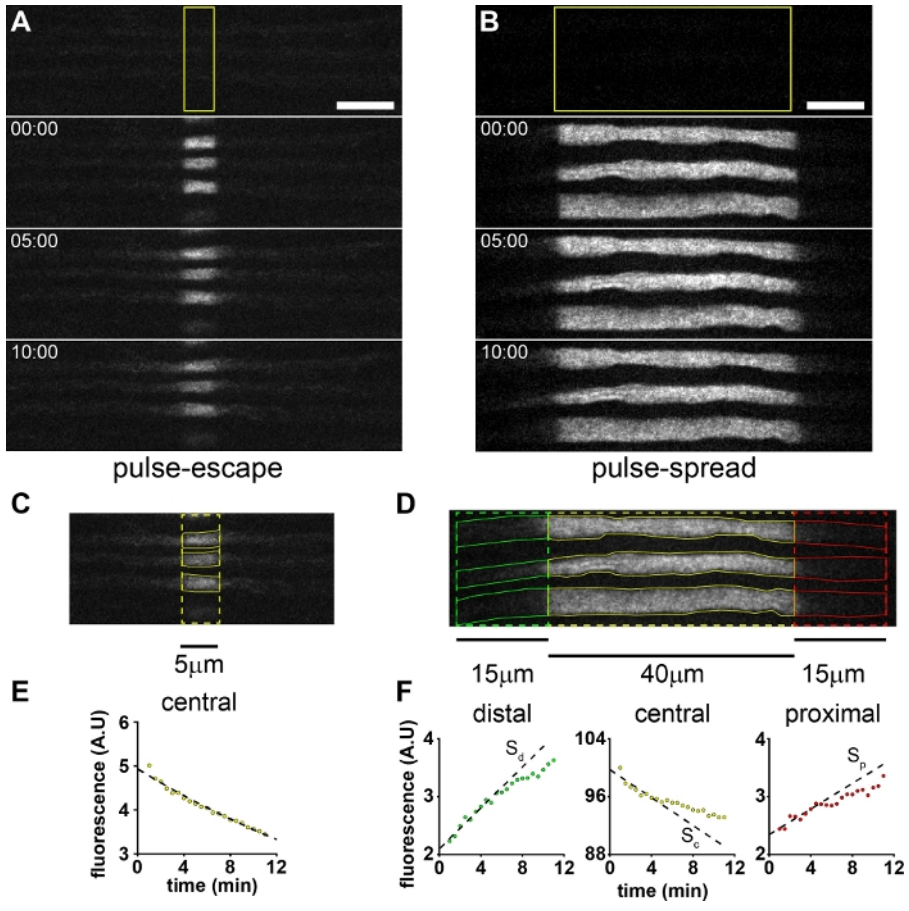

Figure 3: Pulse-escape and pulse-spread experiments. Example of pre-activation, post-activation and timelapse images of myelinated axons in the tibial nerve of an 8 week old mouse in (**A**) a pulse-escape experiment and (**B**) a pulse-spread experiment. Times pre- and post-activation are shown. These activations were performed using 5 scans with a 40 µs pixel dwell time and 5% laser power. Scale bars = 10 µm. (**C**) The measurement ROIs (yellow) for three axons in a pulse-escape experiment. (**D**) The proximal (red), central (yellow) and distal (green) measurement ROIs for three axons in a pulse-spread experiment. The measurement ROIs for each axon are shown in solid red (proximal), solid yellow (central window) and solid green (distal window). (**E**) Plot of the average fluorescence in the three ROIs in C versus time. Dashed line is an exponential function fit to the data, of the form $F_t = Ae^{-\pi t}$, as described previously[7]. F) Plots of the fluorescence in the central, distal and proximal ROIs versus time, average of 14 axons. The slope is calculated from trendlines fit to the first 5 minutes of data.

Please click here to view a larger version of this figure.

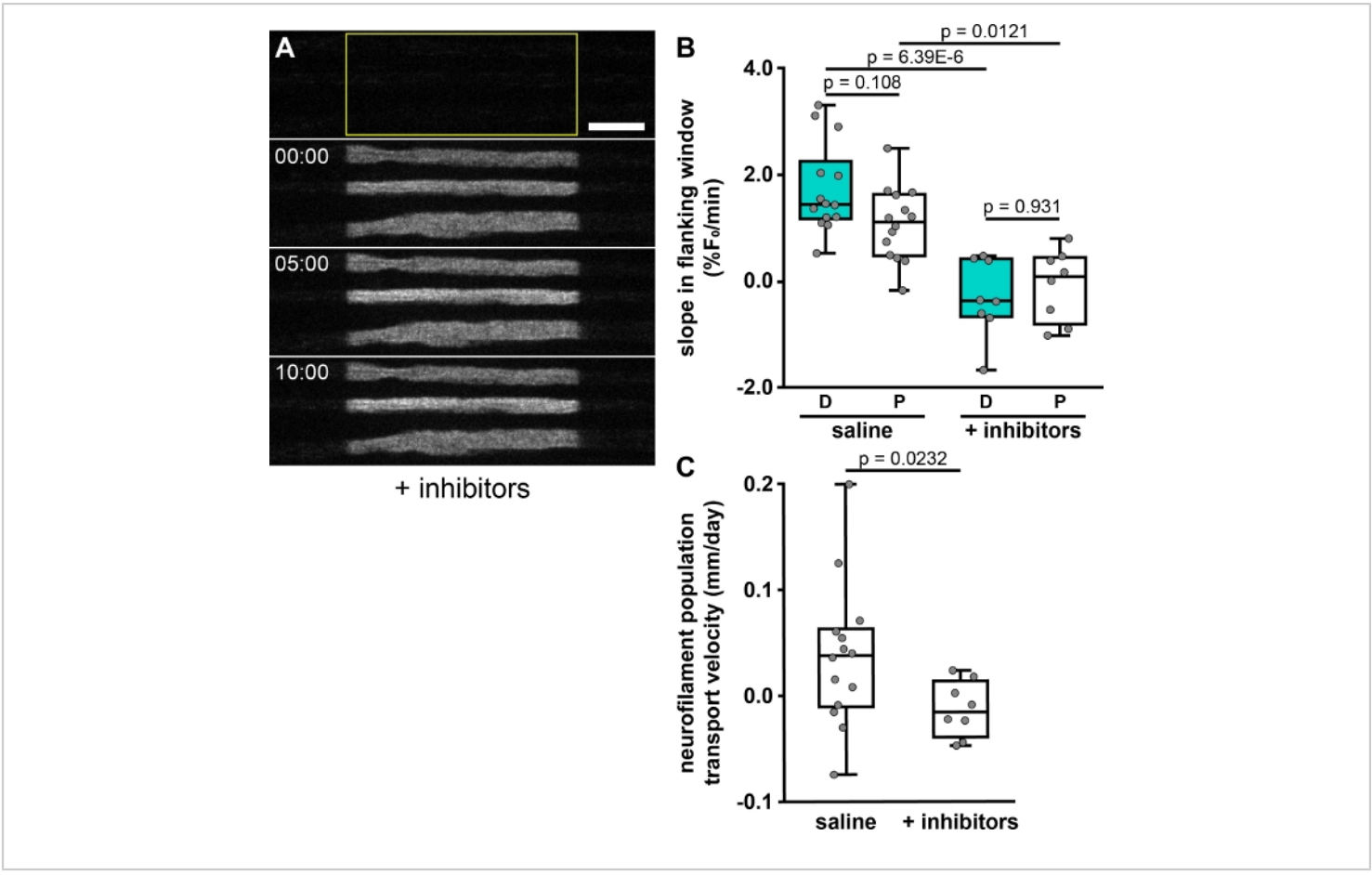

Figure 4: The effect of metabolic inhibitors on neurofilament transport. (**A**) Example of timelapse images of a nerve pretreated with 5.6% (w/v) 2-deoxy-glucose and 0.5 mM sodium iodoacetate to inhibit glycolysis and deplete cellular ATP. Note that the distal and proximal boundaries of the activated regions remain sharp, indicative of an inhibition of neurofilament transport. Scale bar = 10 µm. (**B**) Quantification of distal (D) and proximal (P) neurofilament transport rates (anterograde and retrograde, respectively), expressed as percent of initial fluorescence in the central window (%F_0 /min), from one nerve (14 axons) using standard saline and from two nerves (8 axons) pretreated with saline containing the glycolytic inhibitors. (**C**) Neurofilament population velocities calculated from the directional transport rates, showing a significant decrease in velocity following inhibitor treatment. *** - $p < 0.005$; ** - $p < 0.01$; * - $p < 0.05$. The data show significant impairment of neurofilament transport in the presence of the inhibitors. Please click here to view a larger version of this figure.

Discussion

Care must be taken in the analysis of pulse-escape and pulse-spread experiments because there is significant potential for the introduction of error during the post-processing, principally during the flat-field correction, image alignment and bleach correction. Flat-field correction is necessary to correct for non-uniformity in the illumination, which results in a fall-off in intensity across the field of view from center to periphery. The extent of non-uniformity is wavelength-dependent and thus, should always be performed at the

wavelength that is to be used for acquiring the experimental data. It is important to ensure that the non-uniformity in the flat-field image is truly representative of the non-uniformity in the images to be corrected. Pulse-spread experiments are particularly vulnerable to error from improper flat-field correction because the measurement ROIs extend towards the periphery of the image where the intensity fall-off is greatest.

The optimal paGFP activation settings will vary by activation method and laser parameters, and must be determined empirically before the first imaging session. Too little activation will result in a low signal-to-noise ratio for the activated fluorescence, whereas too much will result in bleaching of the activated fluorescence because both the non-activated and activated paGFP can be excited by violet light. To selectively illuminate a region of interest in the image, we use an Andor FRAPPA laser galvo scanner, which generates a clearly defined region of fluorescence with sharp boundaries, as shown in the Representative Results. We have also had success using an Andor Mosaic Digital Diaphragm, which is a digital micromirror device, with a mercury arc lamp as the illumination source[7]. Other options are commercially available. A challenge when working with paGFP is the delayed increase in fluorescence intensity that happens within 1 minute after the photoactivation step. This increase occurs because illumination with violet light causes a proportion of the activated paGFP molecules to enter a "dark state" from which they can relax back on a time course of tens of seconds[11]. In our experience, the increase is usually less than 5% with widefield excitation but can exceed 20% with laser excitation, which can lead to a significant underestimation of the activated fluorescence. We account for this by acquiring a second "post-activation" image of the paGFP fluorescence 1 minute after photoactivation, and then using this image as the reference point for the subsequent timelapse. However, it is important to recognize that this does introduce another potential source of error in determining the initial fluorescence and the decay kinetics at early times.

Additional attention must be paid to the alignment of the image stacks. The principal source of misalignment is drift or other movement of the specimen during timelapse image acquisition. This can be minimized by using inner gaskets of the appropriate thickness and allowing the preparation to "settle in" before imaging. However, any such delay will reduce the time available for image acquisition since the preparation has a limited window of viability. It is also important to avoid alignment algorithms that warp the image or introduce sub-pixel shifts, as these procedures would resample the pixel intensities in the image. Pulse-spread experiments are particularly vulnerable to errors arising from improper alignment because the borders of the region of activated fluorescence are relatively sharp, and fluorescence in this region is significantly higher than the flanking unactivated regions. If an image is shifted such that a flanking measurement window overlaps the central activated region then the fluorescence intensity in that window will be overestimated. Additionally, the fluorescence increase in flanking windows is typically slow, on the order of 0.05-0.5% of the activated fluorescence in the central window per minute, so small alignment differences between images can result in large jumps in fluorescence values in the distal and proximal measurement windows. Thus, it is imperative that image sets are aligned properly and inspected carefully before proceeding with the analysis.

Correction for photobleaching is necessary to ensure that changes in fluorescence intensity over time accurately reflect changes in the amount of the fluorescent protein. Such

corrections can be a significant source of error in estimating the absolute fluorescence intensities in the central and flanking windows. As photobleaching kinetics depend on the intensity of illumination and the environment of the fluorophore, actual photobleaching rates can vary between sessions and from axon to axon. Thus, it is necessary to measure multiple axons and average the resulting data, which itself introduces some error. The approach described above is to treat the nerve with glycolytic inhibitors and then activate the fluorescence in a region of interest and track the loss of fluorescence intensity over time. The glycolytic inhibitors deplete ATP and thus inhibit neurofilament transport so that the loss of fluorescence is due entirely to photobleaching and not movement of neurofilaments out of the activated region. The average bleaching kinetics determined in this way are then used to correct the experimental data. Since it is not practical to perform a separate bleaching calibration in each imaging session, a single calibration must be applied to multiple sessions spread over many weeks. A disadvantage of this approach is that it does not account for variations in laser power/illumination intensity from day to day, which should therefore be monitored. An alternative approach, which we refer to as “intrinsic bleaching correction”, is to estimate the photobleaching by quantifying the fluorescence in the center of the activated region in the same timelapse movies that are used for the transport measurements. If this measurement region is centrally located and much shorter than the length of the activated region, and then at short times any fluorescent neurofilaments that move out of the measurement region will be replaced by fluorescent neurofilaments that move into it. However, with time the probability of non-fluorescent neurofilaments moving into the measurement region from flanking non-fluorescent regions of the axon increases, leading to an overestimation of the loss of fluorescence due to bleaching. An advantage of this approach is that it corrects for the bleaching characteristics within that same field, but a disadvantage is that the duration of the time window must be determined empirically and will depend on the rate of the transport as well as the length of the activated region. All this having been said, it should be noted that the estimation of the directionality of neurofilament transport using our method is robust to bleaching errors (as it is for flanking window size) because it is given by the ratio of the slopes in the flanking windows and any bleaching correction is a multiplier applied to both numerator and denominator in that calculation.

Due to the noise inherent in a fluorescent system and the potential for additional error added during the image post-processing steps described above, it is important to use large sample sizes for sufficient statistical power. While it is not possible to accurately determine population means, deviations and effect sizes before experimentation, we recommend using the Cohen method[21] assuming a medium effect size and an alpha of 0.05. This results in a Cohen’s **d**, which is the difference in means divided by the pooled standard deviation of both populations, of 0.5, which suggests acquiring at least 105 samples per group. Once this threshold has been reached, one may perform a post hoc power analysis to reassess statistical power in light of actual population measures. Under optimal experimental conditions, it should be possible to obtain from 1-7 analyzable axons (out of 9-20 total axons) per activation, and 5-8 activations per nerve assuming the acquisition of a 10-minute timelapse per activation.

Transgenic mice expressing fluorescent fusion proteins targeted to mitochondria or vesicles have also been used to study axonal transport of membranous organelles in peripheral nerves ex vivo[22,23,24,25]. In addition, the

Schiavo lab has developed approaches to image the axonal transport of retrogradely moving membranous organelles in axons in vivo using fluorescently tagged tetanus toxin fragments, which can be injected into the muscle and are taken up by motor nerve terminals[26]. However, since membranous organelles can be resolved in these axons by fluorescence microscopy, it is possible to analyze the velocity and frequency of their movement directly using timelapse or kymograph analysis. The pulse-escape and pulse-spread methods described here were developed with the specific goal of analyzing the kinetics of neurofilament transport in these axons, in which single neurofilaments cannot be resolved. This requires a population-level analysis over a period of minutes or tens of minutes. We use a transgenic mouse for this purpose, but it should also be possible to express the photoactivatable protein using methods such as viral transduction or in utero electroporation. While the focus has been neurofilament transport, the pulse-escape and pulse-spread methods may also be adapted to study the movement of other cytoskeletal and cytosolic proteins that are transported along axons in the slow components of axonal transport. We also confined the analyses to myelinated axons because their size and myelin sheath allows us to resolve them from their neighbors. Unmyelinated axons cannot be resolved due to their small caliber and tendency to cluster in Remak bundles. We describe the use of tibial nerves ex vivo but the methods should also be applicable to other peripheral nerves that are sufficiently long (>5 mm) and unbranched. In principle, it should also be possible to adapt these methods to image neurofilament transport in vivo (e.g., by surgically exposing a nerve in a sedated mouse and then placing the mouse on a microscope stage).

Disclosures

The authors have nothing to disclose.

Acknowledgments

The authors would like to thank Paula Monsma for instruction and assistance with confocal microscopy and tibial nerve dissection and Dr. Atsuko Uchida, Chloe Duger and Sana Chahande for assistance with mouse husbandry. This work was supported in part by collaborative National Science Foundation Grants IOS1656784 to A.B. and IOS1656765 to P.J., and National Institutes of Health Grants R01 NS038526, P30 NS104177 and S10 OD010383 to A.B. N.P.B. was supported by a fellowship from the Ohio State University President's Postdoctoral Scholars Program.

References

1. Hoffman, P.N., Lasek, R.J. The slow component of axonal transport. Identification of major structural polypeptides of the axon and their generality among mammalian neurons. *Journal of Cell Biology.* **66**, (2), 351-66 (1975).
2. Brown, A. Slow Axonal Transport. *Reference Module in Biomedical Sciences.* doi:10.1016/B978-0-12-801238-3.04765-6 (2014).
3. Wang, L., Ho, C-L., Sun, D., Liem, R.K.H., Brown, A. Rapid movement of axonal neurofilaments interrupted by prolonged pauses. *Nature Cell Biology.* **2**, (3), 137-141 (2000).
4. Uchida, A., Monsma, P.C., Fenn, J.D., Brown, A. Live-cell imaging of neurofilament transport in cultured neurons. *Methods in Cell Biology.* **131**, 21-90 (2016).
5. Trivedi, N., Jung, P., Brown, A. Neurofilaments switch between distinct mobile and stationary states during their

transport along axons. *Journal of Neuroscience.* **27**, (3), 507-16 (2007).

6. Monsma, P.C., Li, Y., Fenn, J.D., Jung, P., Brown, A. Local regulation of neurofilament transport by myelinating cells. *Journal of Neuroscience.* **34**, (8), 2979-2988 (2014).
7. Walker, C.L. et al. Local Acceleration of Neurofilament Transport at Nodes of Ranvier. *Journal of Neuroscience.* **39**, (4), 663-677 (2019).
8. Li, Y., Brown, A., Jung, P. Deciphering the axonal transport kinetics of neurofilaments using the fluorescence photoactivation pulse-escape method. *Physical Biology.* **11**, (2), 026001 (2014).
9. Schindelin, J. et al. Fiji: an open-source platform for biological-image analysis. *Nature Methods.* **9**, 676-682 (2012).
10. Breuer, A.C. et al. Fast axonal transport in amyotrophic lateral sclerosis: an intra-axonal organelle traffic analysis. *Neurology.* **37**, (5), 738-48 (1987).
11. Bancaud, A., Huet, S., Rabut, G., Ellenberg, J. Fluorescence perturbation techniques to study mobility and molecular dynamics of proteins in live cells: FRAP, photoactivation, photoconversion, and FLIP. *Cold Spring Harbor Protocols.* **2010**, (12) (2010).
12. Model, M. Intensity calibration and flat-field correction for fluorescence microscopes. *Current Protocols in Cytometry.* **68** (2014).
13. Schmidt, M.M., Dringen, R. Differential effects of iodoacetamide and iodoacetate on glycolysis and glutathione metabolism of cultured astrocytes. *Frontiers in Neuroenergetics.* **1**, 1-10 (2009).
14. Surre, J. et al. Strong increase in the autofluorescence of cells signals struggle for survival. *Scientific Reports.* **8**, (1), 12088 (2018).
15. Cox, M., Lucey, S., Sridharan, S., Cohn, J. Least Squares Congealing for Unsupervised Alignment of Images. *Proceedings of the IEEE Computer Society Conference on Computer Vision and Pattern Recognition.* doi:10.1109/CVPR.2008.4587573 (2008).
16. Huang, S., Heikal, A.A., Webb, W.W. Two-photon fluorescence spectroscopy and microscopy of NAD(P)H and flavoprotein. *Biophysical Journal.* **82**, (5), 2811-25 (2002).
17. Fenn, J.D., Johnson, C.M., Peng, J., Jung, P., Brown, A. Kymograph analysis with high temporal resolution reveals new features of neurofilament transport kinetics. *Cytoskeleton.* **75**, (1), 22-41 (2018).
18. Alami, N.H., Jung, P., Brown, A. Myosin Va increases the efficiency of neurofilament transport by decreasing the duration of long-term pauses. *Journal of Neuroscience.* **29**, (20), 6625-6634 (2009).
19. Xu, Z., Tung, V.W. Temporal and Spatial Variations in Slow Axonal Transport Velocity Along Peripheral Motoneuron Axons. *Neuroscience.* **102**, (1), 193-200 (2001).
20. Jung, P., Brown, A. Modeling the Slowing of Neurofilament Transport Along the Mouse Sciatic Nerve. *Physical Biology.* **6**, (4), 046002 (2009).
21. Cohen, J. The effect size index: d. *Statistical Power Analysis for the Behavioral Sciences.* Lawrence Erlbaum Associates. **2nd ed.**, 20-26 (1988).
22. Misgeld, T., Kerschensteiner, M., Bareyre, F.M., Burgess, R.W., Lichtman, J.W. Imaging axonal transport of

mitochondria in vivo. *Nature Methods.* **4**, (7), 559-61 (2007).

23. Gilley, J. et al. Age-dependent axonal transport and locomotor changes and tau hypophosphorylation in a “P301L” tau knockin mouse. *Neurobiology of Aging.* **33**, (3), 621.e1-621.e15 (2012).
24. Marinkovic, P. et al. Axonal transport deficits and degeneration can evolve independently in mouse models of amyotrophic lateral sclerosis. *Proceedings of the National Academy of Science of the United States of America.* **109**, (11), 4296-301 (2012).
25. Milde, S., Adalbert, R., Elaman, M.H., Coleman, M.P. Axonal transport declines with age in two distinct phases separated by a period of relative stability. *Neurobiology of Aging.* **36**, (2), 971-81 (2015).
26. Gibbs, K.L., Kalmar, B., Sleigh, J.N., Greensmith, L., Schiavo, G. In vivo imaging of axonal transport in murine motor and sensory neurons. *Journal of Neuroscience Methods.* **257**, 26-33 (2016).